

## BI-DIRECTIONAL PSEUDODYNAMIC TEST OF A FULL-SIZE THREE-STOREY BUILDING

F. J. MOLINA\*, G. VERZELETTI, G. MAGONETTE, PH. BUCHET AND M. GÉRADIN

*Safety in Structural Mechanics Unit, Institute for Systems, Informatics and Safety, Joint Research Centre,  
European Commission, 21020 Ispra (Varese), Italy*

### SUMMARY

The reliability of a Pseudodynamic (PsD) test depends primarily on the accuracy of the control system. Difficulties arise mainly when the method is applied to very stiff or very heavy structures or to structures with a high number of Degrees of Freedom (DoFs). This paper describes the bi-directional PsD testing of a full-size three-storey building. The tested specimen is a composite structure with plan dimensions of  $12 \times 16$  m and height of 9.5 m, made of steel columns and beams combined with composite reinforced concrete slabs. The PsD test included the application of two uncorrelated accelerograms along the horizontal directions  $X$  and  $Y$ . Since the structure was not symmetric about the  $Y$ -axis, the possibility of torsion was considered by taking into account both horizontal displacements and the yaw rotation at every floor. Three displacement-controlled hydraulic actuators were thus used at each floor to impose these three DoFs while a fourth actuator with special control strategy was added to optimize the distribution of loads among the pistons. The validity of the testing methodology was verified by performing also a dynamic random burst test on the specimen which was afterwards pseudodynamically reproduced. Copyright © 1999 John Wiley & Sons, Ltd.

KEY WORDS: pseudodynamic testing; seismic testing; steel-concrete composite structure; bi-directional excitation; torsional response; digital control

### 1. INTRODUCTION

The current lack of knowledge on the behaviour of structures under seismic loading justifies nowadays the execution of large-deformation tests on civil-engineering specimens. Most of them consist of quasi-static cyclic tests or shaking table tests. However, PsD tests<sup>1</sup> may seriously compete with these traditional techniques since they are, in principle, able to combine the advantages of both quasi-static testing, i.e.

- (a) large specimens,
- (b) accurate control and measurement of displacements and forces,

---

\* Correspondence to: F. J. Molina, Safety in Structural Mechanics Unit, ISIS, Joint Research Centre, European Commission, 21020 Ispra (Varese), Italy. E-mail: javier.molina@jrc.it

- (c) easy observation of damage progression and possibility of halting the test procedure,
- (d) substructuring

and shaking table testing, i.e.

- (a) reproduction of dynamic response for specified ground motion.

In practice, since PsD testing is performed quasi-statically with on-line numerical time integration of a discrete system of motion equations, it also has its own specific limitations. In particular:

- (1) The stiffness of the structure should not be large compared to the stiffness of the actuators. A large mass of the specimen may also induce difficulties in the control as it happens even more drastically for a shaking table test. In general, systematic experimental errors (especially control errors) need to be strictly limited in order that the structural response is not significantly altered.<sup>2</sup>
- (2) The discrete model should reproduce properly the response of the distributed-mass structure.
- (3) Specimens made of strain-rate sensitive materials may only be tested if the effect of load application rate is susceptible to a calibrated compensation.<sup>3</sup>

In many real cases, the control system<sup>4,5</sup> developed at European Laboratory for Structural Assessment (ELSA) has allowed successful PsD tests on large specimens which have contributed to a better understanding of the seismic behaviour of such structures.<sup>6</sup> However, as a novelty, the test described in this paper represents the first PsD test performed at the ELSA facility using 3 DoFs per floor. Earlier performed bi-directional PsD tests have already been described in the literature.<sup>7</sup> In particular, Thewalt and Mahin<sup>7</sup> have reported a PsD test on a reduced-scale one-storey model which successfully reproduced the results of a previous shaking table test. Unfortunately, it was not clear whether their testing method could be applied to large size real structures. In fact, they report that, in order to get acceptable accuracy in the control of the PsD test, it was necessary to uncouple most of the real inertial mass (nearly 5 ton) from the specimen.

The general concept of coordinate transformation between actuators and floor generalized DoFs, on which our PsD test has been based, is essentially the same as described by Thewalt and Mahin.<sup>7</sup> However, it differs on the one hand by a rigorous handling of geometric non-linearities in the geometric transformation of forces and displacements and, on the other hand, by introducing the possibility of having more than three actuators and control displacement transducers per floor. Both contributions, together with the unique characteristics of the used control set-up, have allowed to perform, to our knowledge, the first 3-DoF-per-floor PsD test on a large-sized building for strong motion earthquake.

The test structure was a three-storey composite frame with a 3-bay  $\times$  3-bay column layout and overall dimensions of 16  $\times$  12 m in plan and 9.5 m in height (Figure 1). The seismic PsD test as well as the quasi-static cyclic tests performed on the structure at ELSA served for the evaluation of the influence of the concrete slab on the seismic moment capacity for typical beam-column connections. The information obtained is currently being used for the improvement of Eurocode 8.<sup>8-10</sup> Apart from the PsD test performed on the structure for a major earthquake, a small amplitude random burst test was also conducted, both dynamically and pseudodynamically, in order to validate the developed testing methodology.

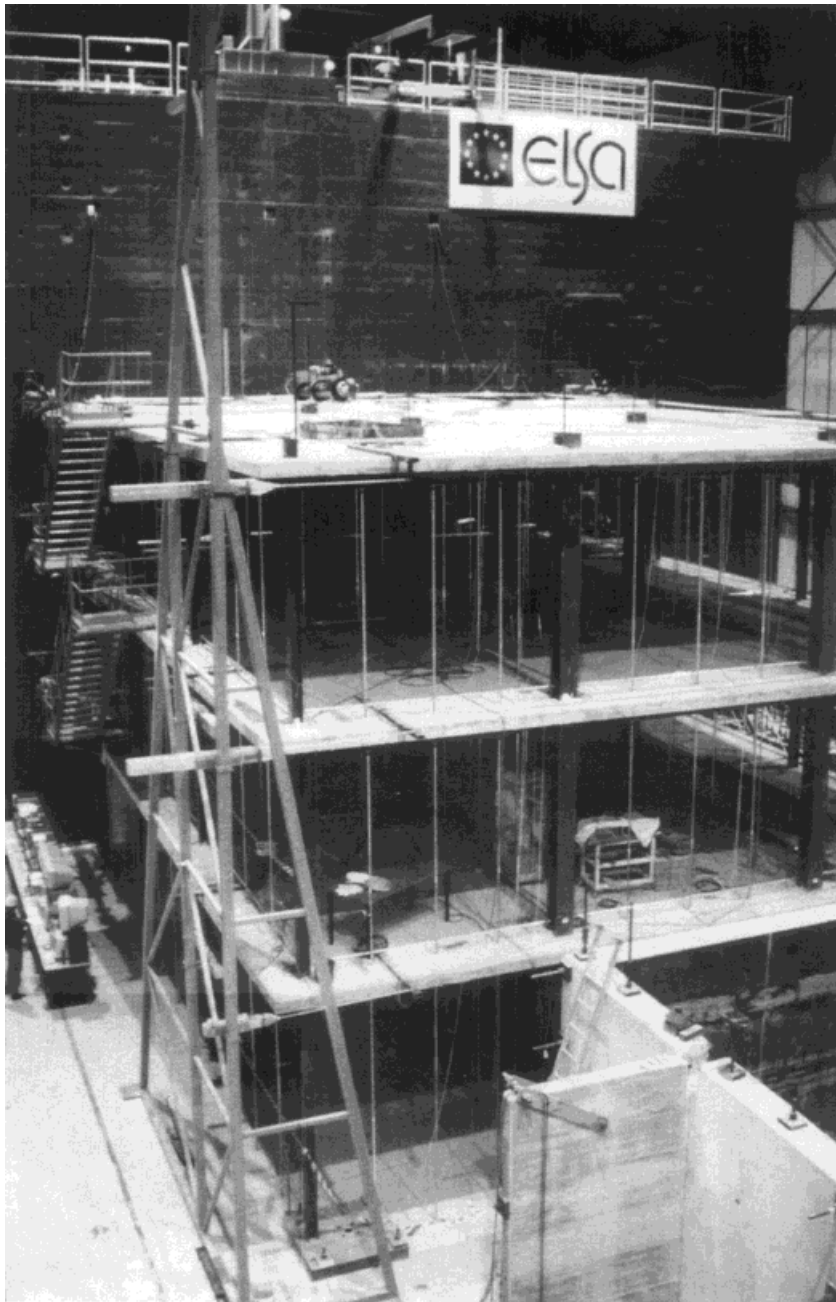


Figure 1. Photograph of the test structure during a PsD test in the ELSA laboratory

## 2. TEST MODELLING FOR 3-DOF FLOORS

The PsD integration of the horizontal response of the structure is performed in terms of three generalized DoFs at each floor consisting of the in-plane displacements  $d_x$ ,  $d_y$  and the rotation  $d_\theta$  at the Centre of Mass (CoM) of the floor with respect to the ground (Figure 2). They are collected in the vector of floor generalized displacements

$$\mathbf{d} = [d_x \quad d_y \quad d_\theta]^T \quad (1)$$

The in-plane resultant forces  $r_x$ ,  $r_y$  and the moment  $r_\theta$  at the CoM are contained in the vector of conjugated generalized restoring forces

$$\mathbf{r} = [r_x \quad r_y \quad r_\theta]^T \quad (2)$$

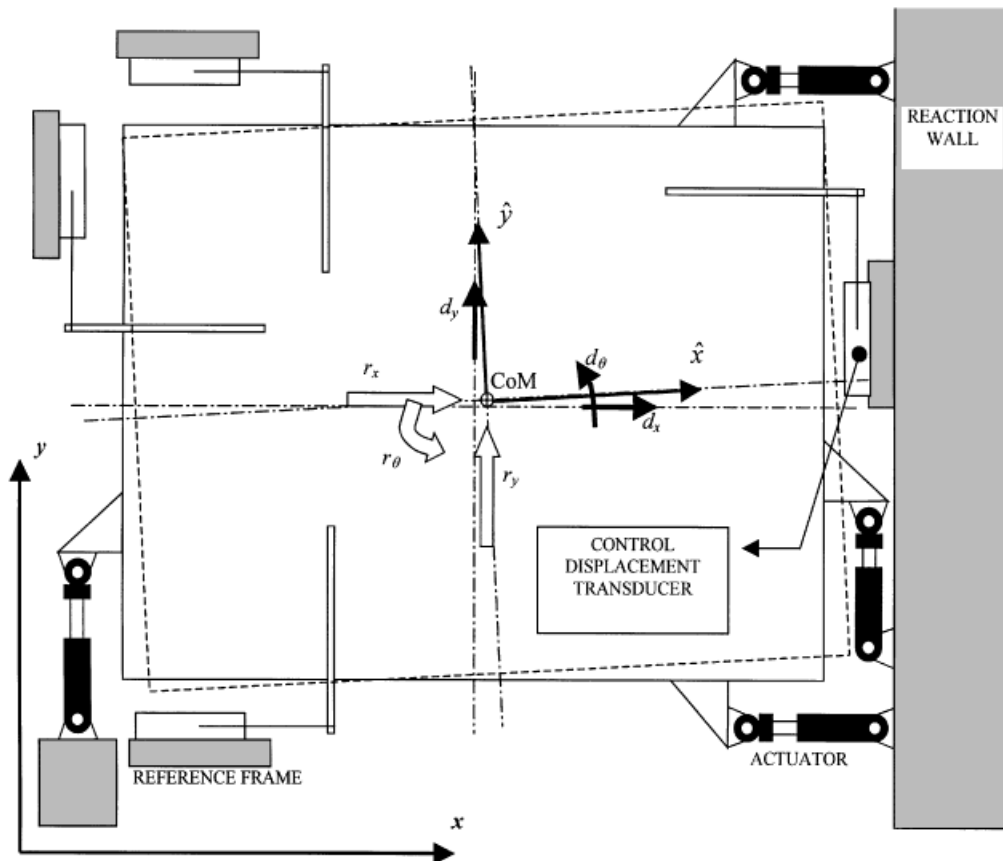


Figure 2. Floor generalized displacements and forces

### 2.1. Equations of motion

Assuming for each floor of the structure a rigid-body behaviour, its horizontal motion is fully described by the generalized displacements (1) and its equations of motion result from the application of D'Alembert's Principle

$$\begin{aligned} -r_x - m(a_x + a_{gx} - y_C a_{g\theta} + z_C a_{g\beta}) &= 0 \\ -r_y - m(a_y + a_{gy} + x_C a_{g\theta} - z_C a_{g\alpha}) &= 0 \\ -r_\theta - I(a_\theta + a_{g\theta}) &= 0 \end{aligned} \quad (3)$$

where the entire structural mass is assumed to be concentrated at the floor level.

Equations (3) may also be expressed in matrix form as

$$\mathbf{m}\mathbf{a} + \mathbf{r} = -\mathbf{m}\mathbf{j}\mathbf{a}_g \quad (4)$$

where the floor mass matrix

$$\mathbf{m} = \begin{bmatrix} m & 0 & 0 \\ 0 & m & 0 \\ 0 & 0 & I \end{bmatrix} \quad (5)$$

contains the floor mass  $m$  and moment of inertia  $I$  at the CoM and

$$\mathbf{a} = [a_x \quad a_y \quad a_\theta]^T = \frac{d^2 \mathbf{d}}{dt^2} \quad (6)$$

is the vector of relative accelerations at the CoM. The vector

$$\mathbf{a}_g = [a_{gx} \quad a_{gy} \quad a_{g\theta} \quad a_{gz} \quad a_{g\beta}]^T \quad (7)$$

appearing at the right-hand side of equation (4) contains the ground accelerations in translations  $x$  and  $y$ , twist  $\theta$ , roll  $\alpha$  and pitch  $\beta$ . The matrix

$$\mathbf{j} = \begin{bmatrix} 1 & 0 & -y_C & 0 & z_C \\ 0 & 1 & x_C & -z_C & 0 \\ 0 & 0 & 1 & 0 & 0 \end{bmatrix} \quad (8)$$

is a geometric influence matrix depending on the current position  $(x_C, y_C, z_C)$  of the CoM.

Thus, the system of equations of motion for the multi-storey structure can be written as

$$\mathbf{M}\mathbf{A} + \mathbf{C}\mathbf{V} + \mathbf{R} = -\mathbf{M}\mathbf{J}\mathbf{a}_g \quad (9)$$

with the matrices

$$\mathbf{M} = \begin{bmatrix} \ddots & & 0 \\ & \mathbf{m} & \\ 0 & & \ddots \end{bmatrix}, \quad \mathbf{A} = \begin{bmatrix} \vdots \\ \mathbf{a} \\ \vdots \end{bmatrix}, \quad \mathbf{R} = \begin{bmatrix} \vdots \\ \mathbf{r} \\ \vdots \end{bmatrix}, \quad \mathbf{J} = \begin{bmatrix} \vdots \\ \mathbf{j} \\ \vdots \end{bmatrix} \quad (10)$$

taking into account the different floors of the building. Here, an assumed viscous damping term  $\mathbf{CV}$  has been added for the sake of generality. Usually, introducing such a damping term is not necessary since, for classical materials, most of the dissipation is of hysteretic type and is thus implicitly taken into account in the restoring forces  $\mathbf{r}$ .

Equations (9) are expressed in terms of generalized forces and displacements. However, the control system used for the test is based on a set of linear actuators and displacement transducers attached at prescribed locations on each floor of the structure. The necessary transformations between both systems of co-ordinates are developed in the following subsections.

## 2.2. Transformation from generalized to transducer displacements

The measurement of the floor displacements for control purposes is achieved using  $n_D \geq 3$  high-resolution linear displacement transducers attached to each floor. As shown in Figure 3, each one of these control displacement transducers consists of a slider  $G_1$ – $G_2$  on which a body  $M$  translates and gives a measure of its relative position on the slider. This slider is attached to a fixed reference frame while the mobile body  $M$  is connected to the measuring point  $D$  on the structure through a pin-jointed rod.

During the test, the computed generalised displacement of the floor is imposed through the actuators with feedback from the displacement transducers. Thus, in order to determine the target displacements at transducer level, a geometric transformation is needed. Starting from a known set of generalized displacements (1), the transformation is obtained through the following steps:

*Step 1:* The position of the floor CoM is updated as

$$\mathbf{S}_C = \mathbf{S}_C^0 + \mathbf{d} \quad (11)$$

where

$$\mathbf{S}_C = [x_C \quad y_C \quad \theta_C]^T \quad (12)$$

are its global co-ordinates and  $\mathbf{S}_C^0$  their reference value for zero displacement. Note that letter  $S$  will in general denote a position in the following formulae.

*Step 2:* The position of the measuring point  $D$  is likewise updated as

$$\mathbf{S}_D = \begin{bmatrix} x_D \\ y_D \end{bmatrix} = \begin{bmatrix} x_C \\ y_C \end{bmatrix} + \mathbf{T}_{\theta_C} \hat{\mathbf{S}}_D \quad (13)$$

where

$$\hat{\mathbf{S}}_D = \begin{bmatrix} \hat{x}_D \\ \hat{y}_D \end{bmatrix} \quad (14)$$

are the co-ordinates of point  $D$  in a reference system local to the floor, centred at its CoM, and

$$\mathbf{T}_{\theta_C} = \begin{bmatrix} \cos \theta_C & -\sin \theta_C \\ \sin \theta_C & \cos \theta_C \end{bmatrix} \quad (15)$$

is a rotation matrix. Assuming an infinitely rigid floor, the local co-ordinates (14) are constant.

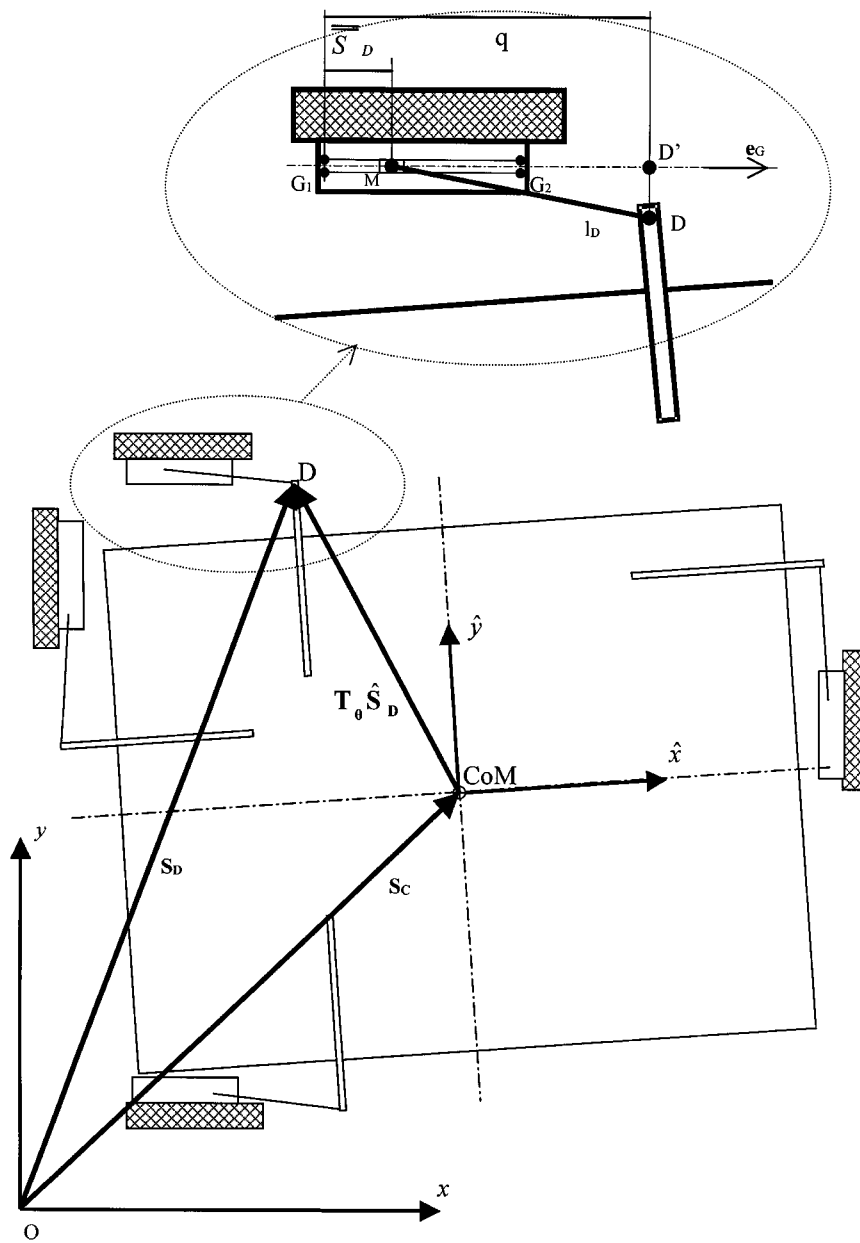


Figure 3. Control displacement transducer

*Step 3:* In order to express the position of body  $M$  (Figure 3) of the transducer along its slider  $G_1$ – $G_2$ , the relative position of the measuring point  $D$  with respect to the slider origin  $G_1$  is computed as

$$\tilde{\mathbf{S}}_D = \overrightarrow{G_1 D} = \mathbf{S}_D - \mathbf{S}_{G_1} \quad (16)$$

Then, the projection of vector (16) along the slider is computed as

$$q = \overrightarrow{G_1 D'} = \tilde{\mathbf{S}}_D^T \mathbf{e}_G \quad (17)$$

where  $\mathbf{e}_G$  is the constant unit vector defined in the direction of positive measurement along the slider. The position of body  $M$  along the slider is then given by

$$\bar{\bar{S}}_D = \overrightarrow{G_1 M} = \overrightarrow{G_1 D'} - \overrightarrow{MD'} = q - \text{sign}(q) \sqrt{l_D^2 - \overrightarrow{DD'}^2} = q - \text{sign}(q) \sqrt{l_D^2 - \tilde{\mathbf{S}}_D^T \tilde{\mathbf{S}}_D + q^2} \quad (18)$$

where  $l_D$  is the constant length of the rod.

The corresponding measure at the transducer is

$$d_D = \bar{\bar{S}}_D - \bar{\bar{S}}_D^0 \quad (19)$$

where  $\bar{\bar{S}}_D^0$  is a reference position for zero displacement of the transducer.

### 2.3. Transformation from actuator to generalized forces

Generally, every displacement transducer is associated with a piston acting approximately along the same axis, but preferably at a point not too close to the measuring point. This is done to avoid the influence on the measurements of local deformations generated by the concentrated load of the piston.

Once the prescribed displacements are achieved, the acting axial force at every actuator is measured by its load cell. However, in order to express these forces as resultant generalized forces at the CoM of the floor, a static transformation is needed. Since the ends of the actuator are pin-jointed, it is assumed that it produces a purely translational force along the line  $PR$  (Figure 4) connecting the ends of the actuator. Starting from the load-cell measure  $r_P$  of this force and assuming that the current position of the floor CoM is known, the transformation results from the following steps:

*Step 1:* The global position of the loading point  $P$  is obtained as

$$\mathbf{S}_P = \begin{bmatrix} x_P \\ y_P \end{bmatrix} = \begin{bmatrix} x_C \\ y_C \end{bmatrix} + \mathbf{T}_{\theta_C} \hat{\mathbf{S}}_P \quad (20)$$

where  $\mathbf{T}_{\theta_C}$  is given by equation (15). Similarly to expression (14),  $\hat{\mathbf{S}}_P$  contains the co-ordinates of point  $P$  in the local reference system to the floor.

*Step 2:* The global components of the piston force are then computed as

$$\mathbf{p}_P = r_P \mathbf{e}_P \quad (21)$$

where  $\mathbf{e}_P$  is a unit vector in the direction of  $\overrightarrow{PR}$ .

*Step 3:* The floor generalized restoring forces (2) are obtained by summing up the effects of all pistons acting on the floor

$$\mathbf{r} = \sum_P \mathbf{T}_P \mathbf{p}_P \quad (22)$$



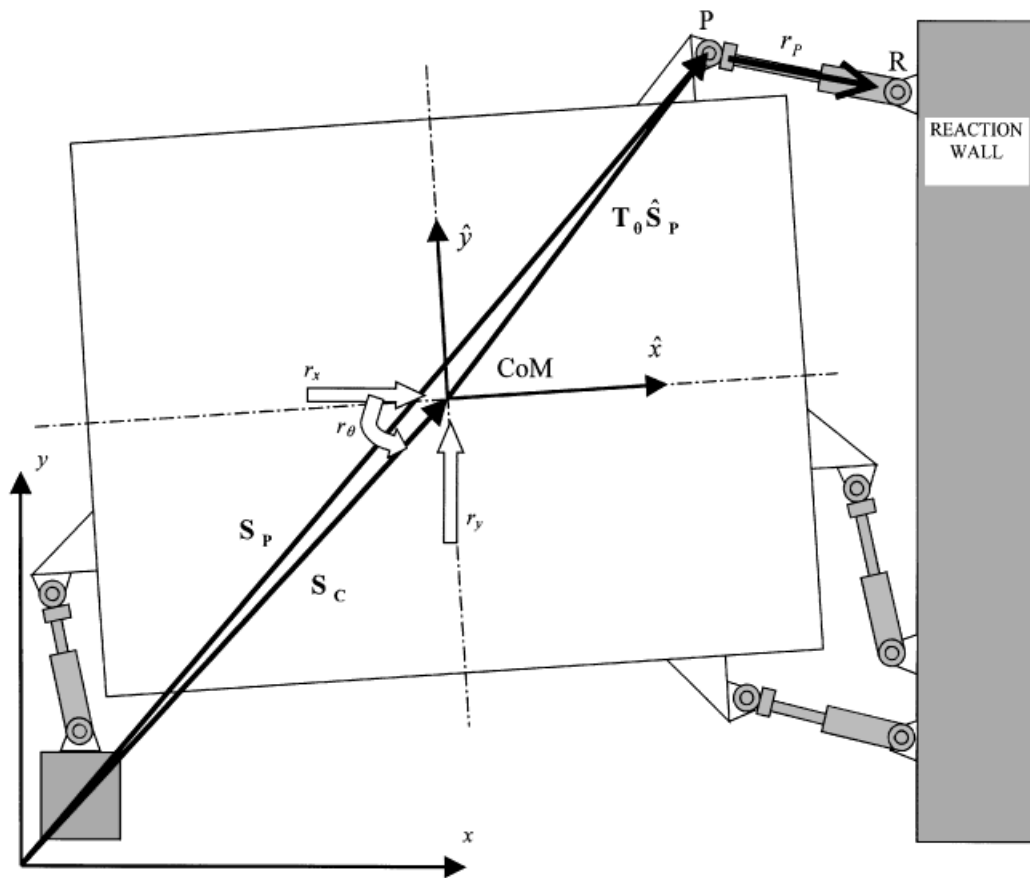


Figure 4. Force applied by the actuator

where

$$\mathbf{T}_P = \begin{bmatrix} 1 & 0 \\ 0 & 1 \\ -y_P & x_P \end{bmatrix} \quad (23)$$

#### 2.4. Estimation of generalized displacements from measured displacements

Due to geometry and control errors and to the flexibility of the floor, the actual displacements and rotation at the CoM differ from the prescribed input. In order to get an estimate of the actual generalized displacements, the measures given by all the control displacement transducers may be exploited as follows:

*Step 1:* Since the relations between generalized and transducer displacements (Section 2.2) are non-linear and cannot easily be inverted in closed form, the solution is achieved through

a Newton–Raphson iteration process starting from a first estimate of the generalized displacements, e.g.

$$\mathbf{d}^{\text{EST}} = \mathbf{0} \quad (24)$$

*Step 2:* The non-linear equations giving the associated transducer displacements  $\mathbf{d}_D$  are obtained by substituting  $\mathbf{d}$  by  $\mathbf{d}^{\text{EST}}$  into equation (11) and applying formulae (11)–(19)

$$\mathbf{d}_D^{\text{EST}} = \mathbf{d}_D(\mathbf{d}^{\text{EST}}) \quad (25)$$

*Step 3:* The difference between the estimate (25) and the measured transducer displacements  $\mathbf{d}_D$  is computed to provide an new estimate of the generalized displacements

$$\mathbf{d}^{\text{EST}} \leftarrow \mathbf{J}^{-1}(\mathbf{d}_D - \mathbf{d}_D^{\text{EST}}) + \mathbf{d}^{\text{EST}} \quad (26)$$

where  $\mathbf{J}$  is the Jacobian matrix

$$\mathbf{J} = \left. \frac{\partial \mathbf{d}_D}{\partial \mathbf{d}} \right|_{\mathbf{d}^{\text{EST}}} \quad (27)$$

computed at  $\mathbf{d}^{\text{EST}}$ . If the number of control transducers on the floor exceeds 3, equation (25) must be solved in a least squares sense, in which case the inverse of  $\mathbf{J}$  in (26) is replaced by the pseudoinverse

$$\text{psinv}(\mathbf{J}) = [\mathbf{J}^T \mathbf{J}]^{-1} \mathbf{J}^T \quad (28)$$

*Step 4:* Steps 2 and 3 are iteratively repeated until a specified tolerance is reached.

## 2.5. Optimal distribution of piston loads

When more than three pistons act on a rigid floor, the use of the individual displacement transducers on the structure as feedback signals for each piston may lead to an unstable control. Hence, it is necessary to use the structural displacements as feedback signals only in number equal to that of DoFs. Then the redundant pistons are controlled by other means in order to maintain an acceptable distribution of loads among all the pistons. This can be done by implementing an algorithm capable of optimizing the distribution of piston loads for a known set of generalized floor loads. Even distribution of forces is also desirable because it leads to a better approximation of the distributed inertial forces of a real dynamic event.

This section describes an algorithm to compute an ‘optimal’ distribution of piston loads compatible with a known set of floor generalized loads. The piston forces determined are assumed to be statically equivalent to the generalized loads while minimizing a penalty function which becomes infinite when a piston force reaches its working limit.

A suitable expression for the penalty function is

$$f(\mathbf{r}_P) = \sum_P \frac{1}{M_P^2 - r_P^2} \quad (29)$$

where  $M_P$  is the working limit of the absolute value of the piston load  $r_P$ . Clearly, minimizing function (29) will guarantee that all piston loads are kept far from their limit. Using expressions (21) and (22), the conditions of static equivalence of the piston loads with the known set of

generalized loads give a constraint on the minimization problem which can be written in the vector form

$$\mathbf{g}(\mathbf{r}_p) = \sum_p \mathbf{T}_p \mathbf{e}_p r_p - \mathbf{r} = \mathbf{0} \quad (30)$$

where  $\mathbf{r}$  is the known set of generalized forces (2). The following constrained minimization problem results

$$\begin{cases} f(\mathbf{r}_p) & \text{minimum} \\ \mathbf{g}(\mathbf{r}_p) = \mathbf{0} \end{cases} \quad (31)$$

By introducing a set of Lagrange multipliers associated with the constraint equations it can be restated in unconstrained form, thus leading to the stationarity condition

$$\frac{\partial h}{\partial \mathbf{x}} = \mathbf{0} \quad (32)$$

of the augmented functional

$$h(\mathbf{x}) = f(\mathbf{r}_p) + \mathbf{g}^T(\mathbf{r}_p) \boldsymbol{\lambda} \quad (33)$$

The solution vector

$$\mathbf{x} = \begin{bmatrix} \mathbf{r}_p \\ \boldsymbol{\lambda} \end{bmatrix} \quad (34)$$

contains as unknowns the piston loads and Lagrange multipliers

$$\boldsymbol{\lambda} = [\lambda_1 \quad \lambda_2 \quad \lambda_3]^T \quad (35)$$

The non-linear equation (32) may be solved by a Newton–Raphson iteration procedure as done previously to obtain the generalized displacements.

### 3. TESTING METHOD

This section describes the time-stepping algorithm used for the time integration of the equation of motion and its application to 3-DoF-per-floor structures using the model described in Section 2. It also describes the implementation of an appropriate control strategy and the characteristics of the software used for the test execution.

#### 3.1. PsD time integration algorithm

This subsection describes the numerical time integration of an equation of motion of the type

$$\mathbf{M}\mathbf{A} + \mathbf{C}\mathbf{V} + \mathbf{R} = \mathbf{F} \quad (36)$$

Equation (36) is a generalization of equation (9) in which  $\mathbf{F}$  is a general external force vector including either seismic equivalent forces or directly applied forces. Two different algorithms are proposed here for its step-by-step integration:

- (1) The Explicit Newmark method, which is equivalent to the Central Difference algorithm, and
- (2) The  $\alpha$  Operator Splitting method, which is a hybrid explicit-implicit method.

Both algorithms can, in fact, be regarded as particular cases of the  $\alpha$ -generalized method, an extension of the Newmark scheme, which can be stated as:<sup>11</sup>

$$\begin{aligned} \mathbf{M}\mathbf{A}_{n+1} + (1 + \alpha)\mathbf{C}\mathbf{V}_{n+1}^* - \alpha\mathbf{C}\mathbf{V}_n^* + (1 + \alpha)\mathbf{R}_{n+1}^* - \alpha\mathbf{R}_n^* &= (1 + \alpha)\mathbf{F}_{n+1} - \alpha\mathbf{F}_n \\ \mathbf{D}_{n+1}^* &= \mathbf{D}_n^* + \Delta t\mathbf{V}_n^* + \Delta t^2\left[\left(\frac{1}{2} - \beta\right)\mathbf{A}_n + \beta\mathbf{A}_{n+1}\right] \\ \mathbf{V}_{n+1}^* &= \mathbf{V}_n^* + \Delta t[(1 - \gamma)\mathbf{A}_n + \gamma\mathbf{A}_{n+1}] \end{aligned} \quad (37)$$

Since the basis for the formulation is available elsewhere,<sup>12,13</sup> the present description will focus only on programming aspects. It will be shown that, operationally, the explicit method can be handled as a particular case of the hybrid one.

Starting with the latter, the  $\alpha$ -Operator-Splitting algorithm is characterized by the coefficients

$$-\frac{1}{3} \leq \alpha \leq 0, \quad \beta = \frac{1 - \alpha^2}{4}, \quad \gamma = \frac{1 - 2\alpha}{2} \quad (38)$$

and defines the implicit approximations to displacements and velocities at time  $n$  as

$$\begin{aligned} \mathbf{D}_n^* &= \mathbf{D}_n + \Delta t^2\beta\mathbf{A}_n \\ \mathbf{V}_n^* &= \mathbf{V}_n + \Delta t\gamma\mathbf{A}_n \end{aligned} \quad (39)$$

Then, by comparison with (37), the explicit predictions of displacements and velocities at time  $n + 1$  can be computed as

$$\begin{aligned} \mathbf{D}_{n+1} &= \mathbf{D}_n^* + \Delta t\mathbf{V}_n^* + \Delta t^2\left(\frac{1}{2} - \beta\right)\mathbf{A}_n \\ \mathbf{V}_{n+1} &= \mathbf{V}_n^* + \Delta t(1 - \gamma)\mathbf{A}_n \end{aligned} \quad (40)$$

They are explicit in the sense that they are computed solely from the information at the previous step. They are also the ones that are imposed on the structure and for these the restoring forces

$$\mathbf{R}_{n+1} = \mathbf{R}(\mathbf{D}_{n+1}) \quad (41)$$

are measured. The method assumes that the difference between explicit and implicit forces is small and can be approximated by a linear model

$$\mathbf{R}_{n+1}^* - \mathbf{R}_{n+1} = \mathbf{R}(\mathbf{D}_{n+1}^*) - \mathbf{R}(\mathbf{D}_{n+1}) \approx \mathbf{K}_I(\mathbf{D}_{n+1}^* - \mathbf{D}_{n+1}) \quad (42)$$

in which  $\mathbf{K}_I$  is an implicit stiffness matrix which preferably overestimates the initial stiffness of the structure.

Starting from the known initial values  $\mathbf{D}_1$ ,  $\mathbf{V}_1$ ,  $\mathbf{A}_1$ , at time step  $n = 1$  ( $t = 0$ ), the successive computation stages of the method at every time step are:

*Stage 1:* Compute at instant  $n$  the implicit displacements and velocities  $\mathbf{D}_n^*$ ,  $\mathbf{V}_n^*$  using equations (39).

*Stage 2:* Compute next at instant  $n + 1$  the explicit values of displacements and velocities  $\mathbf{D}_{n+1}$ ,  $\mathbf{V}_{n+1}$  using equations (40).

*Stage 3:* Impose on the structure the new explicit displacement  $\mathbf{D}_{n+1}$  and measure the associated restoring force (41).

*Stage 4:* Increment the step counter  $n \leftarrow n + 1$ .

*Stage 5:* Compute the acceleration at new time  $n$  from the equilibrium equation

$$\mathbf{A}_n = \tilde{\mathbf{M}}^{-1}[(1 + \alpha)(\mathbf{F}_n - \mathbf{R}_n - \mathbf{C}\mathbf{V}_n) - \alpha(\mathbf{F}_{n-1} - \mathbf{R}_{n-1} - \mathbf{C}\mathbf{V}_{n-1}) + \alpha(\gamma\Delta t\mathbf{C} + \beta\Delta t^2\mathbf{K}_I)\mathbf{A}_{n-1}] \quad (43)$$

with

$$\tilde{\mathbf{M}} = \mathbf{M} + (1 + \alpha)(\gamma\Delta t\mathbf{C} + \beta\Delta t^2\mathbf{K}_I) \quad (44)$$

*Stage 6:* Go back to stage 1 until the final time is reached.

Similarly, the Explicit Newmark algorithm is defined by the coefficients

$$\alpha = 0, \quad \beta = 0, \quad \gamma = \frac{1}{2} \quad (45)$$

and the same stages 1–6 can then be performed as for the Operator-Splitting algorithm. The advantage in this case is that no implicit stiffness matrix is required. The disadvantage is that the algorithm is only conditionally stable, imposing thus small time steps compared to the minimum period of the structure.

### 3.2. Marching procedure

The application of the time integration method in the 3-DoF-per-floor model described in Section 2 yields the following experimental step-by-step procedure. The algorithm starts from known initial values  $\mathbf{D}_1$ ,  $\mathbf{V}_1$ ,  $\mathbf{A}_1$  and the computations are organized in the following stages:

*Stage 0:* Let  $n = 0$ .

*Stage 1:* Transform the generalized displacements into target displacements  $\mathbf{d}_D$  at the control transducers

$$(\mathbf{d}_D)_{n+1}^{\text{TARGET}} = \mathbf{d}_D(\mathbf{D}_{n+1}) \quad (46)$$

computed from the geometric model described in Section 2.2.

*Stage 2:* Send these target displacements (46) to the controllers which impose them on the specimen by performing a ramp from the previous position.

*Stage 3:* Let  $n \leftarrow n + 1$ .

*Stage 4:* Measure the current displacements  $(\mathbf{d}_D)_n^{\text{MEAS}}$  and restoring loads  $(\mathbf{r}_P)_n$  at the controllers,  $\mathbf{r}_P$  being the forces applied by the pistons.

*Stage 5:* From the measured control displacements, estimate the current generalized displacements on each floor

$$\mathbf{D}_n^{\text{MEAS}} = \mathbf{D}((\mathbf{d}_D)_n^{\text{MEAS}}) \quad (47)$$

using the least-squares solution described in Section 2.4.

*Stage 6:* From the measured piston forces, compute the current generalized restoring forces

$$\mathbf{R}_n = \mathbf{R}((\mathbf{r}_P)_n, \mathbf{D}_n^{\text{MEAS}}) \quad (48)$$

using the transformation formulae of Section 2.3.

Stage 7: If  $n > 1$ , compute the new accelerations

$$\mathbf{A}_n = \mathbf{A}_n(\mathbf{F}_n, \mathbf{R}_n, \mathbf{V}_n, \mathbf{F}_{n-1}, \mathbf{R}_{n-1}, \mathbf{V}_{n-1}, \mathbf{A}_{n-1}) \quad (49)$$

using expression (43).

Stage 8: Predict the generalized displacement and velocity at the next time increment

$$(\mathbf{D}_{n+1}, \mathbf{V}_{n+1}) = f(\mathbf{D}_n, \mathbf{V}_n, \mathbf{A}_n) \quad (50)$$

using the finite-difference approximations (39) and (40) of the integration algorithm.

Stage 9: Go back to stage 1 until reaching final time.

### 3.3. Control strategy

As already mentioned in Section 2.5, using more than three actuators per floor in order to have a better distribution of forces may lead to difficulties in the control strategy. Let us assume that PID controllers are used and that three actuators are controlled using as feedback one displacement transducer on the structure. In this case, there are, in principle, three options in the choice of the feedback transducer to control the redundant actuators: first, the 'closest' displacement transducer on the structure (as for the other three actuators), second, the actuator load cell and, third, the actuator internal displacement transducer.

The first option is not practicable because the control system becomes unstable for acceptable controller gains. In fact, if the system turned out to be stable and accurate for this configuration, it would mean that the floor is relatively flexible and that more than three degrees of freedom could be taken into account.

The second option may lead to a stable control system, but, usually, force control strategies do not produce the best accuracy. In fact, its accuracy is much lower than the one that would be obtained with only three pistons and using the structural displacements as feedbacks. This second option could be acceptable for a cyclic test, but not for a PsD test in which relatively small control errors may result in a large distortion of the integrated response.<sup>2</sup>

The third option may give at the same time an accurate and stable control system owing to being a displacement control strategy, as in the first option, but associated with a transducer which sees a more flexible subsystem than the structure itself. In fact, the displacements measured by the internal transducer of the actuator are considerably larger than the structural ones since they comprise the deformation of the reaction wall and actuator attachments. Furthermore, in this case, feedback between co-located quantities is achieved.

Thus, we have adopted the actuator internal transducers as feedbacks for the redundant pistons. The only potential problem with this option is that the load distribution remains undetermined. To solve it, the computed target for the redundant pistons is slightly adjusted at every integration step in order to control the distribution of loads on the floor. Instead of using expression (46), their target is computed as

$$(d_p)_{n+1}^{\text{TARGET}} = d_p(\mathbf{D}_{n+1}) + (\bar{d}_p)_{n+1} \quad (51)$$

where the first term on the right-hand side is the theoretical elongation of the piston and the second one is a correction introduced in order to modify the force. It is updated at every time step in the form

$$(\bar{d}_p)_{n+1} = (\bar{d}_p)_n + \frac{(r_p^{\text{OPTIMUM}} - r_p^{\text{MEASURED}})_n}{K_p} \quad (52)$$

where the term added to the correction is the difference between the computed optimum force of the piston (Section 2.5) and the measured one at the former step, divided by a stiffness parameter  $K_p$  empirically selected. In general terms, the smaller the parameter, the faster is the convergence of the force to the optimum value. However, using too small a value may result in instability which would make the force to oscillate out of control in very few steps.

### 3.4. Hardware and software set-up

The servo-control units used for these tests were MOOG actuators with  $\pm 0.5$  m stroke and load capacity of 0.5 MN, except for the third floor of the specimen where the three actuators closer to the main reaction wall had a capacity of 1.0 MN. The control displacement transducers on the structure were optical HEIDENHEIN sensors with a stroke of  $\pm 0.5$  m and a 2  $\mu$ m resolution. Every actuator was equipped with a strain-gauge load cell and a TEMPOSONIC internal displacement transducer. Each actuator had its own PID controller based on a 486DX4 processor. The characteristics of this hardware have been fully described by Magonette<sup>4,5</sup>.

All the controllers are connected to a master unit by means of an EFIWAY net. For the previous PsD tests performed at the ELSA, this master unit assumed two tasks:

*Task 1:* sending the targets to the controllers and receiving and displaying the associated measurements.

*Task 2:* performing all computations for the PsD integration.

The corresponding software (based on C language) had to combine real-time capabilities with high-level logic and algebraic computation. However, for this occasion, due to the significant complexity added by the 3-DoF-per-floor model, this master unit has been divided into two units:

- (a) a communication unit in charge of task 1 and
- (b) a computation unit in charge of task 2.

These two units are separated processors, which can communicate at a very high-speed owing to a dual-RAM interface module. The computation unit consists of an NT workstation running the testing procedure in MATLAB interpreted language, while the communication unit is a DOS PC running the real-time application in C. The advantage of this task splitting is that the interpreted language offers much more flexibility (and simplicity of programming and debugging) for high-level operations and user interface. On the other hand, the interpreted language is not able to perform the real-time tasks still reserved to the communication unit working in C.

This configuration allowed developing a software which implemented the described model and marching procedure with the following capabilities:

- (1) PsD integration either by Explicit Newmark or  $\alpha$ -Operator-Splitting algorithms.
- (2) *Pause* and *Continue* buttons.
- (3) Possibility of on-line change of parameters such as excitation spans, step minimum duration and ramp speed, alarm limits, control-strategy parameters such as  $K_p$  (see Section 3.3).
- (4) Possibility to restart from any previous time step or initial conditions.
- (5) Possibility of substituting the real specimen by a linear model for checking purposes.
- (6) Graphic monitoring of controller co-ordinates, generalized co-ordinates, energy variables, deformed shape or any other programmed function.
- (7) Centralized alarm protection based on actuator and transducer limits, which is also applied to the target before it is sent.

## 4. DESCRIPTION OF TEST CAMPAIGN

### 4.1. Test specimen

The test structure was a 3-storey steel-concrete composite building constructed within the ELSA laboratory. Its overall dimensions were  $16 \times 12$  m in plan and 9.5 m in height. It had four frames (1, 2, 3, 4) in the  $X$  (EW) direction, four frames (A, B, C, D) in the  $Y$  (NS) direction and three floors (see Figure 5). Frames 2 and 3 in the  $X$  direction and frames A and B in the  $Y$  direction were moment-resisting frames. The frames were made of standard Fe360 rolled sections, while the floors consisted of a 15-cm slab of reinforced C30/37 concrete poured on corrugated metal decking. The structure is representative of current European construction methods and the design has been made according to Eurocode 8. Different slab designs in the beam-column regions were introduced to study the effect of the resulting composite behaviour in the beam-to-column moment transfers. More details on the design can be found in the references.<sup>8–10</sup>

### 4.2. Instrumentation

In addition to the load cells and control displacement transducers of the four actuators used for each floor, resistor strain gauges and potentiometer displacement transducers were used, yielding 550 channels of continuous acquisition in total, each one sampling one averaged measure at every test step. The strain gauges were stuck on the columns in order to measure the bending moment in  $X$  and  $Y$  directions at two sections and the axial load at one section. The displacement transducers were used to measure at every beam the vertical deflection at three points as well as the relative horizontal displacements between the columns in  $X$  and  $Y$  directions at each slab level. These data have been used in the post test analysis either directly, in the form of moment-rotation diagrams for every joint, or indirectly, by means of the identification of a numerical model which assesses the plastic rotation at the beam joints.

### 4.3. Test programme

Initially, three cyclic tests were performed on the specimen, each one with increasing amplitude up to a nominal global drift of 2 per cent (180 mm of displacement at the third floor). The first quasi-static cyclic test was executed in the  $X$  direction, the second one in the  $Y$  direction and the third one as a combination of both directions. Afterwards, the PsD seismic test described below was performed. The intensity of this test was chosen so that the response would not exceed the drift values of the previous cyclic tests. Finally, a major quasi-static cyclic test was conducted in the  $X$  direction with amplitude up to 420 mm or 4.7 per cent of global drift. After this test, the global strength fell by 30 per cent and the lower beam flanges at many of the joints in the  $X$  direction were fractured. Afterwards, a small-amplitude dynamic random-excitation test was performed followed by its PsD reproduction in order to check the validity of the PsD modelling and testing methodology. The results of the cyclic tests have been described and analysed by Bouwkamp *et al.*<sup>9</sup> The seismic and random tests are described in the next two subsections.

### 4.4. PsD seismic test

The steel-concrete composite structure had been designed according to Eurocode 8 with a design spectrum characterized by 5 per cent of damping ratio, a behaviour factor  $q = 6$  and



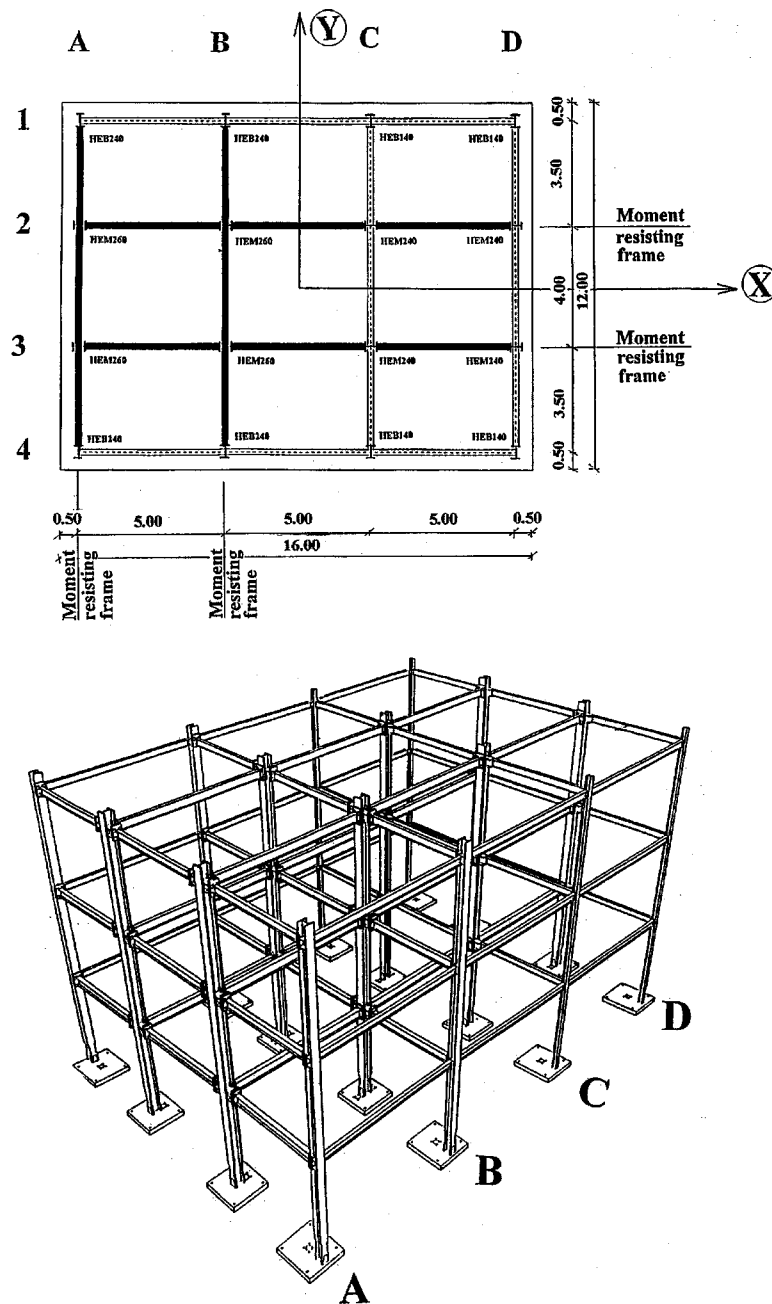


Figure 5. Views of the test structure

a soil profile B. For the PsD seismic test, two independent artificial accelerograms with a duration of 10 s were used for the  $X$  and  $Y$  directions. The intensity of the normalized spectra was multiplied by 2.25 so that the peak ground acceleration was  $2.25 \text{ m/s}^2$  in both directions (Figure 6). All the rotational components of the ground acceleration vector (7) were considered zero.

The 9-DoF equation of motion for the PsD test has the form described in Section 2.1 with translational and rotational masses of

$$m = 124 \times 10^3 \text{ kg}, \quad I = 4464 \times 10^3 \text{ kg m}^2 \quad (53)$$

for every floor. These masses do not correspond to the mass of the specimen but to the design mass relating to the earthquake action. The viscous damping has been considered as negligible, all the dissipation being thus introduced hysteretically by the experimental restoring forces.

The algorithm used for the integration was the Explicit Newmark, as described in Section 3.1, with a time increment of 0.005 s. Since the maximum frequency was estimated to be under 10 Hz, such time increment is small enough to guarantee stability and accuracy without an excessive number of time steps. The control strategy used for the imposition of the displacements at every floor was the one described in Section 3.3. With two actuators acting in the  $X$  direction and two other in the  $Y$  direction, one of the actuators in the  $X$  direction was indirectly controlled in order to optimize the force distribution, while the other three were directly fed back by their control displacement transducers on the structure.

Some of the results of this PsD seismic test are shown in Figures 7 and 8. In Figure 7, the three curves represent the displacements at the three floors in  $X$  direction (upper graph),  $Y$  direction (middle) and torsion  $\theta$  (lower). The maximum generalized displacement was 120 mm and was recorded at the CoM of the third floor in the  $X$  direction. However, the maximum displacement at the control transducers (not plotted in the figure) was 200 mm. It was recorded in the East transducer at the third floor (the torsion centre of the structure being closer to its West end). Thus, although no rotational ground motion was introduced, an important torsional response took place due to the lack of symmetry of the structure, especially in the  $Y$  direction.<sup>15</sup>

Figure 8 shows the base shear versus top displacement cycles obtained in the three directions. Although the test did not produce severe damage, some plastic dissipation is observed from these curves. On the other hand, each one of these graphs contains in fact two curves. The solid line corresponds to the base shear computed from the piston forces, while the dashed line corresponds to base shear computed from the strain-gauge bridges attached to the columns. The vicinity of both curves provides a check of the excellent reliability of these strain-gauge measurements.

The effect of hysteretic dissipation can be better quantified in Figure 9, where the absorbed energy

$$E_a = \int \mathbf{r}^T d\mathbf{d} \quad (54)$$

is plotted as a function of time, splitting the three directions ( $X$ ,  $Y$  and  $\theta$ ) and the total. The absorbed energy (54) may be calculated either from the measured displacements or from the computed ones. In the first case it represents the energy really dissipated by the specimen—apart from measurement errors—while in the second case it represents the apparent energy as observed by the integration algorithm which computes the response. If the difference, or error energy,

$$E_e = \int \mathbf{r}^T d(\mathbf{d}^{\text{MEASURED}} - \mathbf{d}^{\text{ALGORITHM}}) = \int \mathbf{r}^T d(\varepsilon) \quad (55)$$

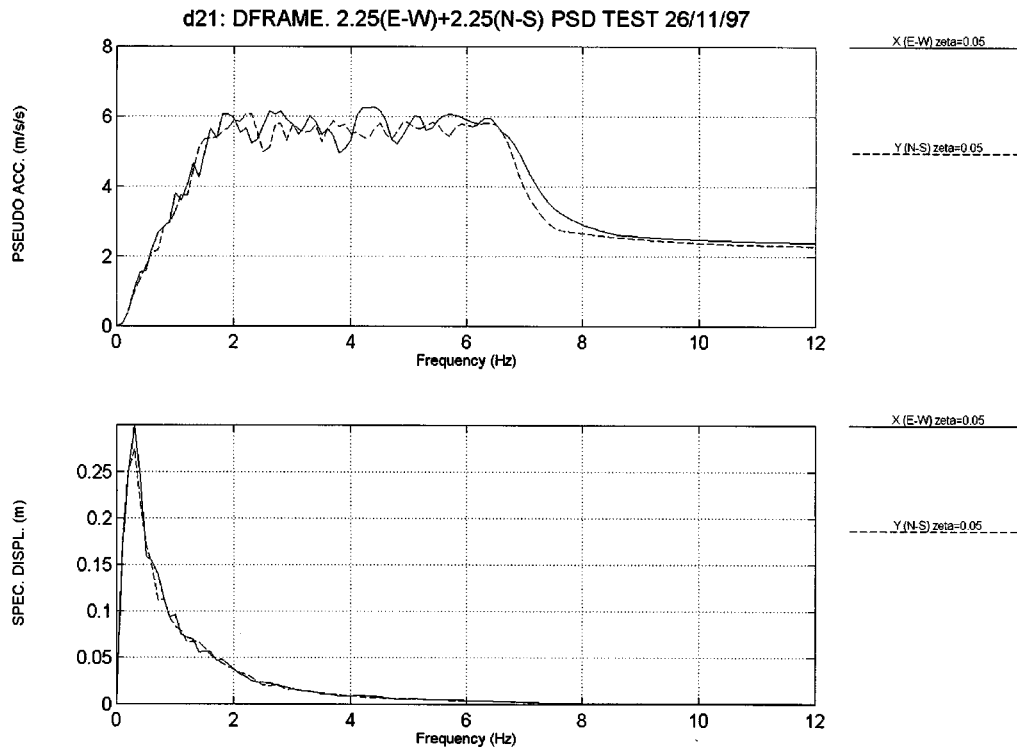


Figure 6. Response spectra of the ground accelerograms

is large in relation to the total energy (54), the PsD response obtained should not be accepted as representative of that specimen. This could occur due to inadequate quality of the control system or to an excessive testing velocity. The error energy (55) obtained within this PsD test is plotted at the lower part of Figure 9; it is negative and amounts to 6 per cent of the total dissipated energy. This means that the specimen really dissipated only 94 per cent of the energy apparent to the PsD integration. In other words, the specimen has in reality an effective damping of about 0.94 times the damping shown in the PsD integration (in this respect, some identified apparent damping values are shown in Figure 10).

Another interesting result of this seismic test is shown in Figure 10. It consists of the eigen frequencies and modes as obtained by a transfer function method applied to the input accelerograms and output displacements. The method is based on a time-domain identification of a filter model, which has already shown to be well adapted for PsD results.<sup>14</sup> Using the response during the entire earthquake (2000 discrete time instants), a linear 9-DoF model was adjusted by a minimization of the square error. Considering different orders (2, 4, 6, ...) for the model, a good convergence was found for the values shown in the figure. Since the real structure behaves non-linearly, these linear-equivalent results depend on the amplitude of the response as well as on the time interval; this last effect is due to the damage accumulation. Consequently, the values shown should be considered as an average during the entire earthquake and may characterise the

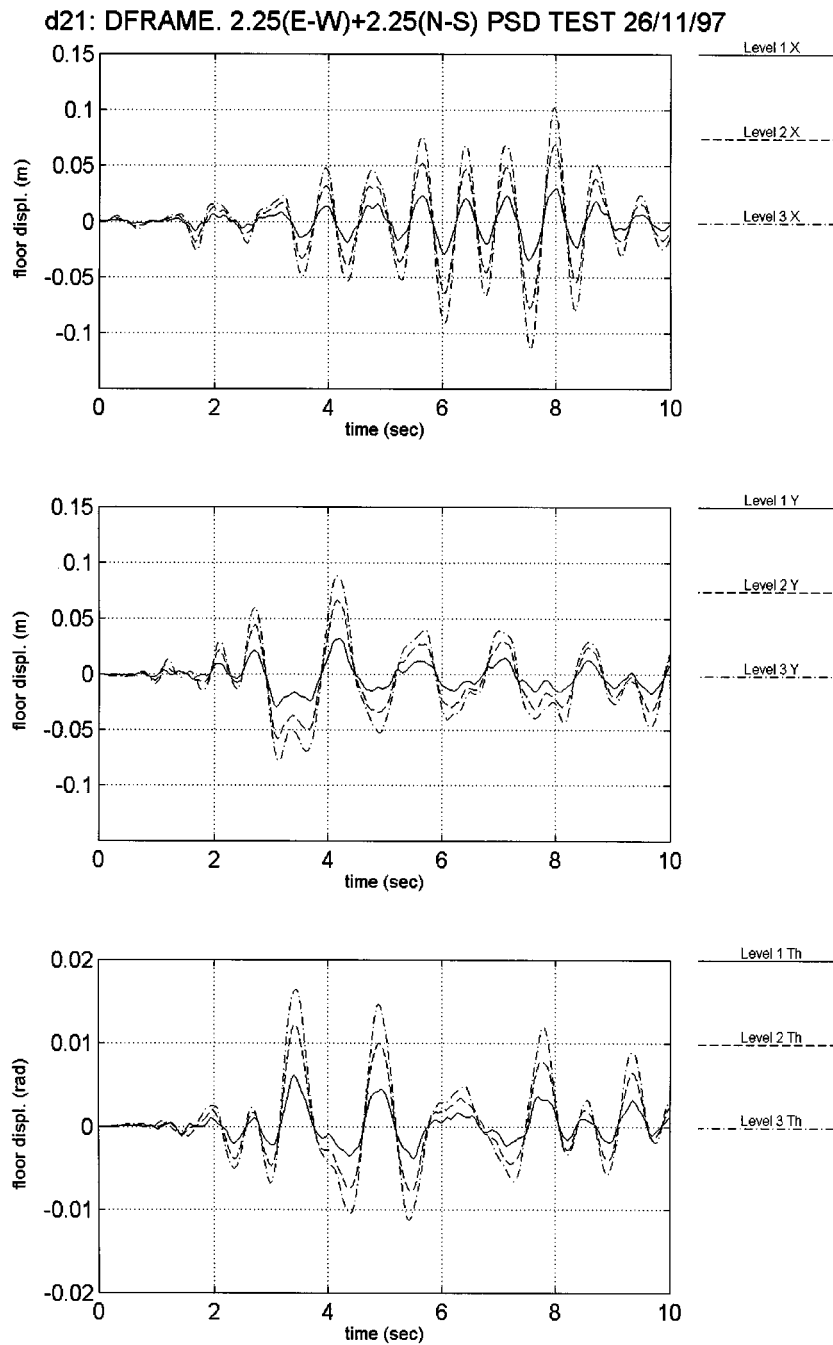


Figure 7. Seismic test: floor generalized displacements in  $X$  (upper),  $Y$  (middle) and  $\theta$  (lower graph) directions

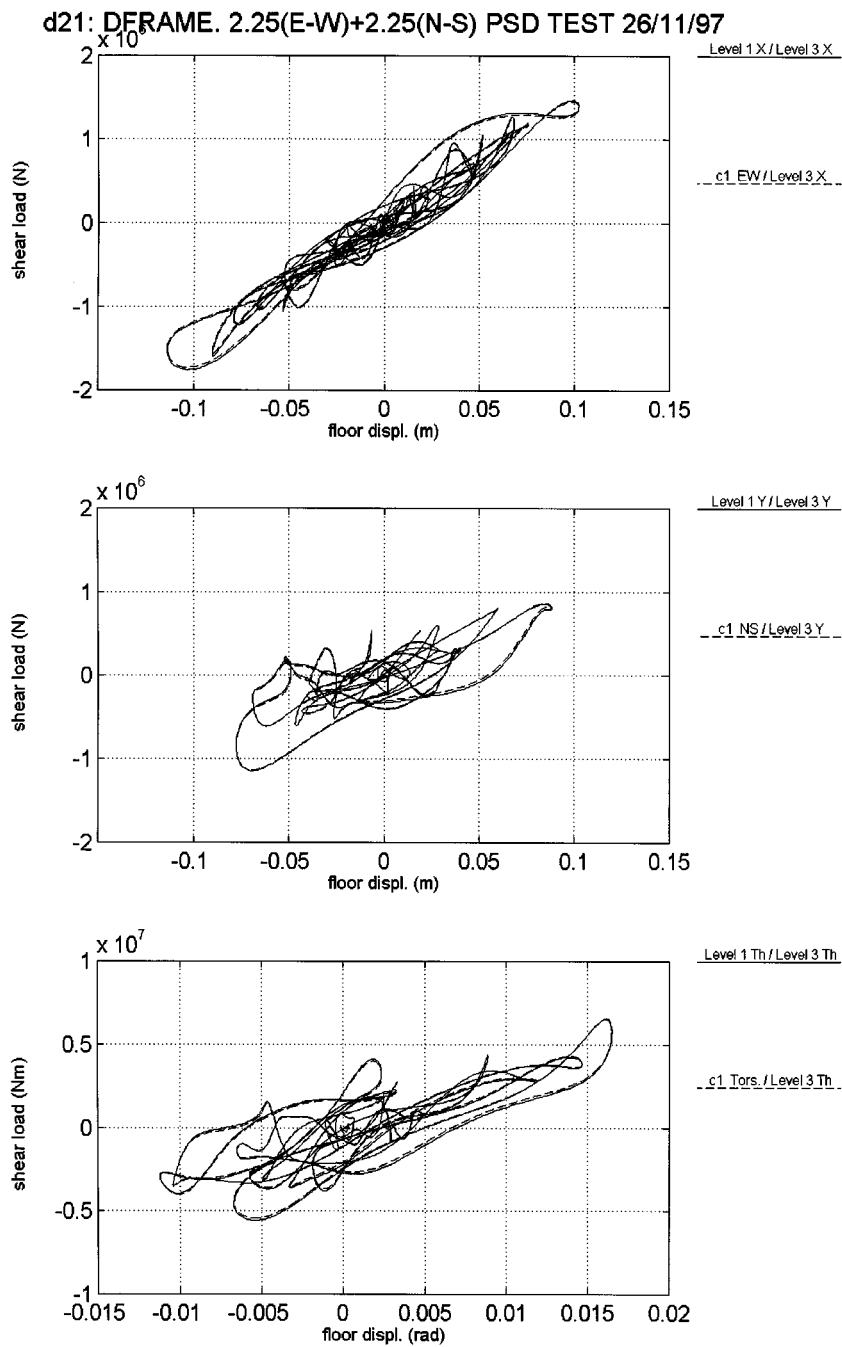


Figure 8. Seismic test: base shear-top displacement cycles in  $X$  (upper),  $Y$  (middle) and  $\theta$  (lower graph) directions

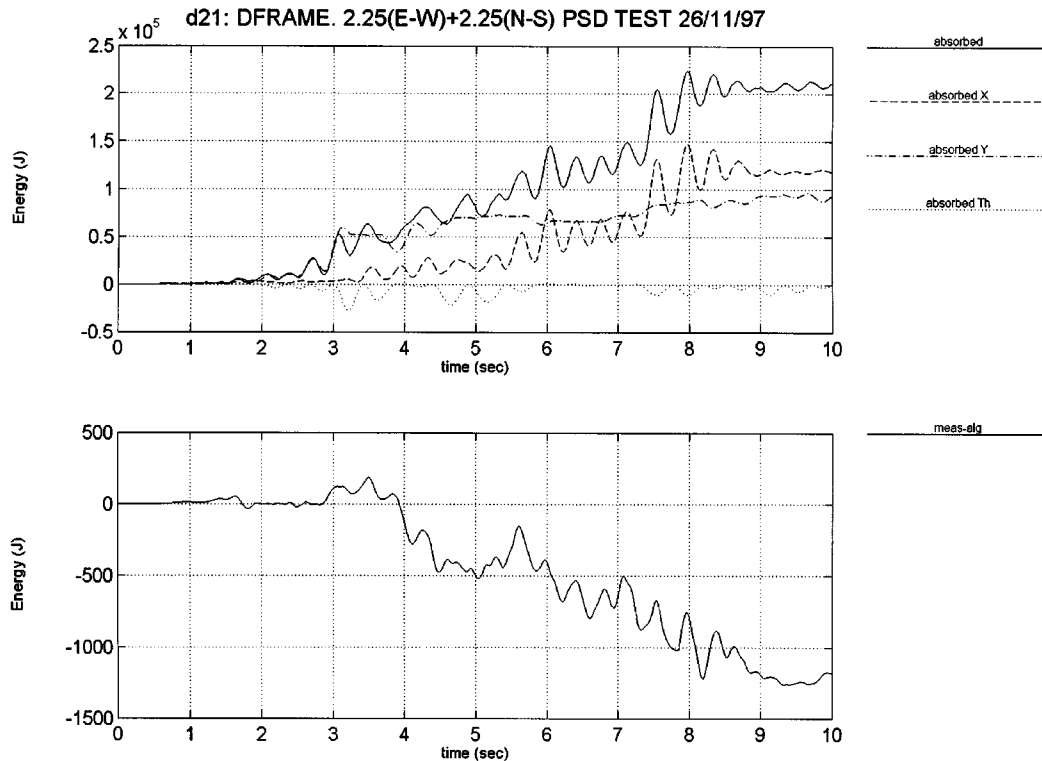


Figure 9. Seismic test: absorbed energy (upper) and error energy (lower graph)

response of the structure, in its current degradation state, to earthquakes with similar spectra and intensities as the one used for the input. Looking at the form of the displacement response spectrum (Figure 6) a significant response was to be expected for the first three modes. The predominance of the lower frequencies is also clearly seen in Figure 7.

#### 4.5. Random burst test

After the main tests on the building specimen had been conducted, all fragile instrumentation was removed and a real dynamic random-burst test was performed. This small-amplitude dynamic test was reproduced subsequently by a PsD test in order to verify the validity of the bi-directional PsD testing methodology. The advantage of this type of dynamic check test is that it uses the same loading set-up as the PsD test.

For the dynamic test, 9 statistically independent reference signals were generated for nine pistons acting on the structure, using the actuator internal displacement transducer as feedback. The reference signals had a significant content up to 12 Hz, but, due to the limitations of the loading devices at high frequencies, the measured applied forces were intense only for frequencies up to 10 Hz. The response at the control displacement transducers was measured at a sampling period of 0.005 s. The generalized displacements obtained at the third floor are shown in

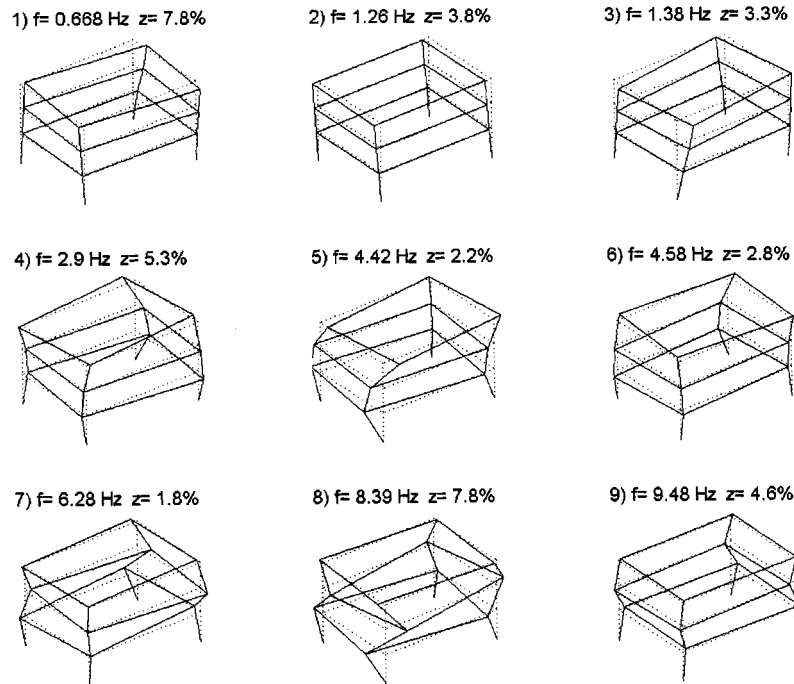


Figure 10. Seismic test. Identified linear-equivalent natural frequencies, damping ratios and mode shapes

Figure 11. The maximum displacement in the  $X$  direction at the CoM of the floor was about 6 mm, while in the  $Y$  direction it was about 12 mm.

For the PsD test, the same methodology as for the seismic test was applied, except for the seismic equivalent forces which were substituted by the external forces  $\mathbf{F}$  in equation (36) which were in fact the ones measured during the dynamic test.

The mass introduced was the one estimated for the specimen, or:

$$\begin{array}{lll}
 \text{1st floor:} & m = 68 \times 10^3 \text{ kg} & I = 2680 \times 10^3 \text{ kg m}^2 \\
 \text{2nd floor:} & m = 65 \times 10^3 \text{ kg} & I = 2620 \times 10^3 \text{ kg m}^2 \\
 \text{3rd floor:} & m = 72 \times 10^3 \text{ kg} & I = 2710 \times 10^3 \text{ kg m}^2
 \end{array} \quad (56)$$

Under these conditions, the PsD test was performed twice with the results shown in Figure 11, where a comparison is made with the dynamic test. The results show the extent to which the PsD tests are capable of acceptably reproducing the shape and especially the maximum of the dynamic response. The discrepancies observed with respect to the dynamic curves may be mainly attributed to the damage accumulation in the specimen under repeated tests. This could occur even for such small amplitudes because, unfortunately, at this stage the specimen showed already major cracks at critical points.

## d26: DFRAME. DYNAMIC RANDOM BURST TEST. 4/12/97

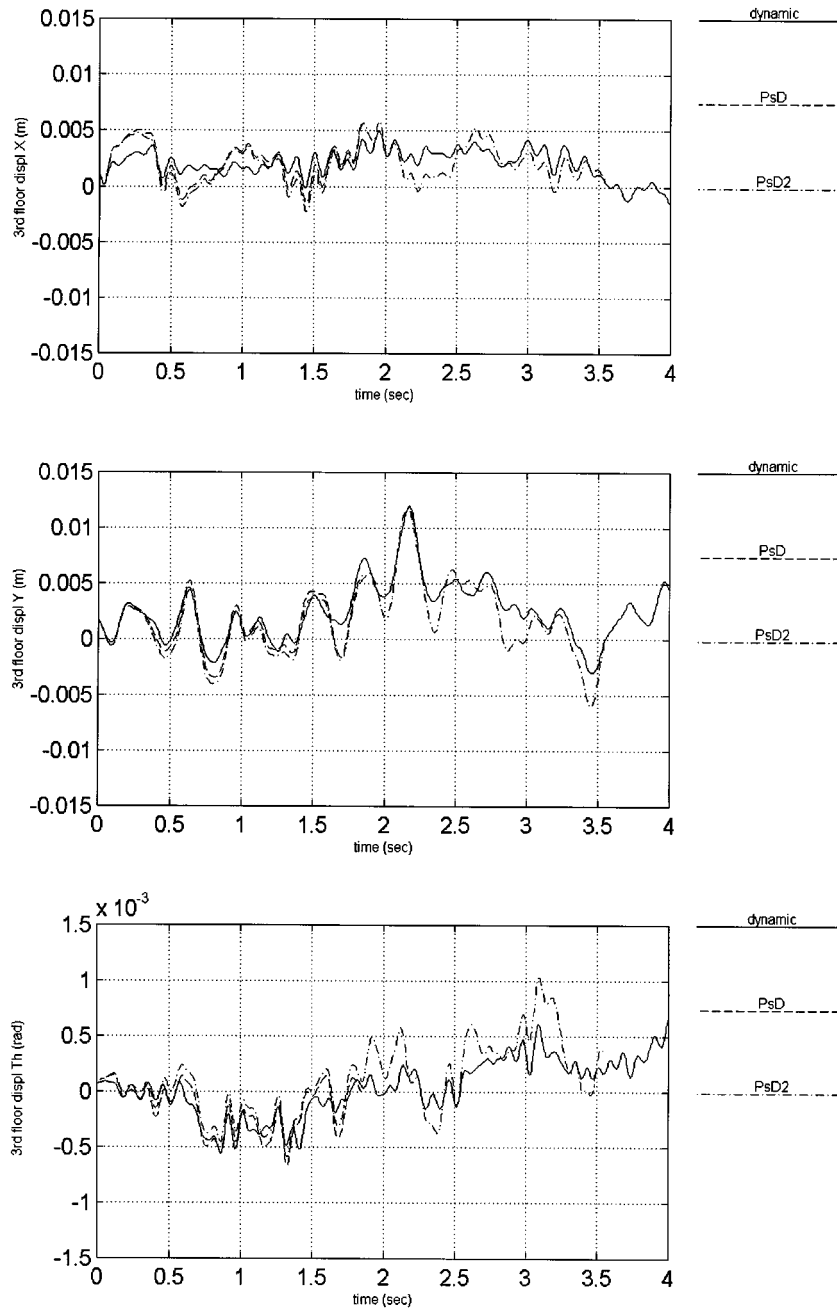


Figure 11. Random burst test: dynamic and PsD displacements at the third floor in  $X$  (upper),  $Y$  (middle) and  $\theta$  (lower graph) directions



## 5. CONCLUSIONS

The PsD testing technology has been successfully extended to bi-directional excitation of real-size buildings by implementing the test modelling and procedure described in the paper. Some important features of the methodology are:

- (a) The capability of imposing large displacements by means of a rigorous geometrically non-linear transformation between actuator co-ordinates and floor generalized co-ordinates.
- (b) The ability to use more than three actuators and control displacement transducers per floor by applying a stable and accurate control strategy which guarantees a suitable distribution of the forces among the actuators.
- (c) The development of a new, flexible software structure through separation of high-level tasks and real-time tasks which communicate through a dual-RAM interface module. The high-level tasks, comprising the geometric transformation and the time integration, are written in MATLAB (interpreted language) while the real-time tasks are programmed and compiled in C.

The performed seismic test on a three-storey steel-concrete composite building gave useful information about the seismic behaviour of that type of structure and served to show the applicability of the proposed testing technology for large-size specimens. The random burst test executed dynamically and pseudodynamically on that specimen provided information on the reliability of the PsD methodology.

## ACKNOWLEDGEMENTS

The work described herein was funded partly by DG III of the European Commission and partly by ICONS, a research network financed by the TMR programme of the European Commission. The project was developed by cooperation with the Joint Research Centre, ISIS, Structural Mechanics Unit, ELSA at Ispra (Italy), the University of Technology at Darmstadt (Germany) and the University of Liege (Belgium). We thank the personnel of the ELSA laboratory for their enthusiastic collaboration without which these tests would not have been possible.

## REFERENCES

1. K. Takanashi and M. Nakashima, 'A state of the art: Japanese activities on on-line computer test control method', *Report of the Institute of Industrial Science*, Vol. 32, No. 3, University of Tokyo, 1986.
2. P. B. Shing and S. A. Mahin, 'Cumulative experimental errors in pseudo-dynamic tests', *Earthquake Engng. Struct. Dyn.* **15**, 409–424 (1987).
3. F. J. Molina, E. Gutierrez, G. Magonette, V. Renda, D. Tirelli and G. Verzeletti, 'Pseudo-dynamic simulation of base isolation on a reinforced concrete building by means of substructuring', *Proc. 1st European Conf. on Structural Control*, 1996.
4. G. Magonette, 'Digital control of pseudo-dynamic tests', in J. Donea and P. M. Jones (eds.), *Experimental and Numerical Methods in Earthquake Engineering*, Kluwer Academic Publishers, Dordrecht, 1991, pp. 63–69.
5. G. Magonette, P. Pegon, F. J. Molina and Ph. Buchet, 'Development of fast continuous substructuring tests', *Proc. 2nd Word Conf. on Structural Control*, 1998.
6. J. Donea, G. Magonette, P. Negro, P. Pegon, A. Pinto and G. Verzeletti, 'Pseudo-dynamic capabilities of the ELSA laboratory for earthquake testing of large structures', *Earthquake Spectra* **12**(1), 163–180 (1996).
7. C. R. Thewalt and S. A. Mahin, 'Non-planar pseudo-dynamic testing', *Earthquake Engng. Struct. Dyn.* **24**, 733–746 (1995).
8. J. G. Bouwkamp, H. Parung, S. Qorraj, A. Plumier and C. Doneux, 'Research on the energy dissipation capacity of composite steel/concrete structures', *Final Report of Contracts No. 11708-96-03 ED ISP D and 11708-96-03 ED ISP B* European Commission, Joint Research Centre, Ispra, 1998.

9. J. G. Bouwkamp, H. Parung and A. Plumier, 'Bi-directional cyclic response study of 3-D composite frame', *Proc. XIth European Conf. on Earthquake Engineering*, 1998.
10. A. Plumier, C. Doneux, J. G. Bouwkamp and C. Plumier, 'Slab design in connection zone of composite frames', *Proc. 11th European Conf. on Earthquake Engineering*, 1998.
11. H. M. Hilber, T. J. R. Hughes and R. L. Taylor, 'Improved numerical dissipation algorithms in structural dynamics', *Earthquake Engng. Struct. Dyn.* **5**, 283–292 (1977).
12. M. Nakashima, T. Akawaza and O. Sakaguchi, 'Integration method capable of controlling experimental error growth in substructure pseudo-dynamic test', *J. Struct. Constr. Engng. AIJ* **454**, 61–71 (1993) (in Japanese).
13. D. Combescure and P. Pegon, 'Alpha-operator splitting time integration technique for pseudo-dynamic testing error propagation analysis', *Special Publication No. 1.94.65*, European Commission, Joint Research Centre, Ispra, 1994.
14. F. J. Molina, P. Pegon and G. Verzeletti, 'Time-domain identification from seismic pseudodynamic test results on civil engineering specimens', *Proc. 2nd Int. Conf. on Identification in Engineering Systems*, The Cromwell Press Ltd, 1999.
15. P. Negro and F. J. Molina, 'Bi-directional pseudodynamic tests on a three-storey, full-scale composite asymmetric building', *2nd European Workshop on the Seismic Behaviour of Asymmetric and Set-Back Structures*, 8–10 October 1999, Istanbul.